

Article

# Ni-Based Composites from Chitosan Biopolymer a One-Step Synthesis for Oxygen Evolution Reaction

Behzad Aghabarari <sup>1,2</sup>, José Manuel Luque-Centeno <sup>2</sup>, Maricarmen Capel-Sánchez <sup>2</sup>,  
Maria Jesús Lázaro Elorri <sup>3</sup>  and Maria Victoria Martínez-Huerta <sup>2,\*</sup>

<sup>1</sup> Department of Nanotechnology and Advanced Material, Materials and Energy Research Center (MERC), Tehran, PO box 14155-4777, Iran; b.aghabarari@merc.ac.ir

<sup>2</sup> Instituto de Catálisis y Petroleoquímica, CSIC, Marie Curie 2, E28049 Madrid, Spain; jmluque@icb.csic.es (J.M.L.-C.); mcapel@icp.csic.es (M.C.-S.)

<sup>3</sup> Instituto de Carboquímica, CSIC, Miguel Luesma Castán 4, E50018 Zaragoza, Spain; mlazaro@icb.csic.es

\* Correspondence: mmartinez@icp.csic.es

Received: 12 April 2019; Accepted: 17 May 2019; Published: 21 May 2019

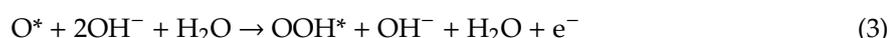


**Abstract:** Cost-efficient and sustainable electrocatalysts for oxygen evolution reaction (OER) is highly desired in the search for clean and renewable energy sources. In this study, we develop a new one-step synthesis strategy of novel composites based on Ni and molybdenum carbide embedded in N- and P-dual doped carbon matrices using mainly chitosan biopolymer as the carbon and nitrogen source, and molybdophosphoric acid (HMoP) as the P and Mo precursor. Two composites have been investigated through annealing a mixture of Ni/chitosan and HMoP with two unlike carbon matrices, melamine and graphene oxide, at a high temperature. Both composites exhibit similar multi-active sites with high electrocatalytic activity for OER in an alkaline medium, which is comparable to the IrO<sub>2</sub> catalyst. For this study, an accurate measurement of the onset potential for O<sub>2</sub> evolution has been used by means of a rotating ring-disk electrode (RRDE). The use of this method allows confirming a better stability in the chitosan/graphene composite. This work serves as a promising approach for the conversion of feedstock and renewable chitosan into desired OER catalysts.

**Keywords:** oxygen evolution reaction; composites; chitosan; graphene; nickel; molybdenum carbide

## 1. Introduction

Electrochemical water splitting from renewable energy (wind- or solar-derived electricity) is of particular interest because it is considered a clean and sustainable process [1,2]. The efficiency of electrochemical water splitting is dependent on two half reactions, in other words, the oxygen evolution reaction (OER) at the anode and the hydrogen evolution reaction (HER) at the cathode [3,4]. However, the kinetics of the OER in a four-electron and four-proton process are sluggish, and therefore the development of effective OER electrocatalysts is critical to increase the overall water splitting efficiency. Theoretical models suggest that the OER progresses in four steps in alkaline medium as follows [5,6]:



Currently, state-of-the-art oxygen evolution catalysts require noble metal-based electrocatalysts, such as Ir and Ru oxides, which are costly and have insufficient earth-abundance to be utilized for

extensive industrial applications [7–9]. Therefore, not only is it desirable to develop new materials of low cost and suitable activity, but also consider the sustainable utilization of renewable material maximizing its conversion into high value products such as electrocatalysts.

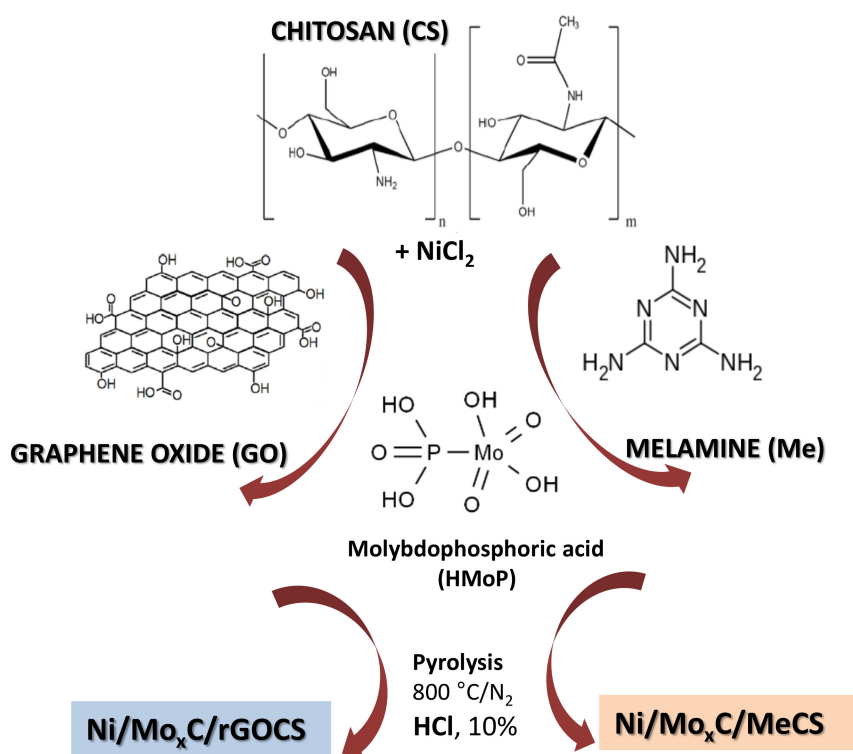
In recent years, an extensive variety of transition metals including Co, Ni, Fe, and their compounds have been explored for the OER catalysts [6,10–15]. Among them, Ni-containing materials, such as nickel oxides, nickel hydroxides, and nickel-metal alloys have been given special attention because of their abundance and their good water oxidation potential [3,11–14,16,17]. Furthermore, some reports have shown that coupling molybdenum carbide with Ni significantly improves the OER performance [13,18,19]. For example, Ni<sub>2.0</sub>Mo<sub>0.26</sub>@N-carbon nanostructures have shown excellent OER electrocatalytic performances which are mainly attributed to the synergistic effect between  $\gamma$ -MoC and Ni heterostructures [13]. In situ electro-oxidation studies during the OER have shown that Mo<sub>2</sub>C-based catalysts are converted to Mo oxides which have been demonstrated to be active for OER [20,21]. Furthermore, the presence of heteroatoms, such as B and N, could increase its activity and stability upon in situ oxidation of Mo<sub>2</sub>C [22]. Notably, coupling transition metal species with N-doped carbon-based materials is one of the most popular strategies for tailoring active and durable advanced composite electrocatalysts. These compounds combine unique properties, such as high electrical conductivity and enhanced electron transfer, ascribed to the N incorporation into the carbon matrix with a modulated distribution of charge density [8,23].

Herein, we considered the sustainable utilization of chitosan (CS), a derivative of the waste products of the crabbing and shrimp canning industries, in combination with graphene or melamine for the preparation of high-value N-doped carbon materials [24–26]. Chitosan is a renewable polymer, naturally abundant and low cost, which has outstanding properties such as biodegradability, non-toxicity, and excellent stability [23,26–28]. Recently, S. Selvam et al. [28] have synthesized graphene oxide-chitosan-copper crosslinked composites. They have showed that the hydroxyl and amine groups of the CS are good ligands to coordinate with carboxylic groups from graphene oxide (GO). Melamine is also a nitrogen-enriched organic molecule and inexpensive raw material in the chemical industry [24,29,30]. Melamine possesses a three-dimensional monoclinic structure which is similar to C<sub>3</sub>N<sub>4</sub>, which decomposition favours for the incorporation of nitrogen in the carbon materials obtained by pyrolysis [24].

In this work, two nickel and molybdenum-based N- and P-dual doped carbon composites were prepared in a simple and new one-step strategy through annealing the Ni precursor and molybdophosphoric acid (HMoP) with a mixture of chitosan with two different carbon matrices, melamine and graphene oxide. HMoP was used as a source of P and Mo. Influence of the carbon matrix on morphology, structure, and nitrogen and phosphorous doping degree has been investigated. Linear sweep voltammetry was performed to evaluate the activity of the catalysts toward the oxygen evolution reaction in alkaline medium. Furthermore, an accurate measurement of the onset potential of O<sub>2</sub> evolution was performed using a rotating ring-disk electrode (RRDE). The nature of the active sites of the electrocatalysts was discussed based on various physical and chemical characterizations. Both composites exhibited enhanced electrocatalytic activity for the OER in an alkaline medium, being similar to the IrO<sub>2</sub> catalyst. In addition, the unique nature of graphene material improved the electrochemical properties of the multi-active site composite, Ni/Mo<sub>x</sub>C/rGOCS, showing higher electrochemical durability.

## 2. Results and Discussion

The synthetic strategy is schematically illustrated in Scheme 1. The chitosan composites electrocatalysts were prepared with a loading chitosan of 50 wt%. The mixture of chitosan polymer, carbon matrix, and transition metals were pyrolyzed at 800 °C in a tubular furnace. Then, the samples were cooled to room temperature under N<sub>2</sub> to obtain the desired composites.



**Scheme 1.** Schematic illustration of the formation of composites.

Figure 1 shows the X-ray diffraction (XRD) patterns of the Ni/Mo<sub>x</sub>C/rGOCS and the Ni/Mo<sub>x</sub>C/MeCS catalysts. Both composites showed diffraction peaks assigned to Ni (JPCDS 00-001-1258), Mo<sub>2</sub>C (JPCDS 00-035-0787), and MoC (JPCDS 00-045-1015). Diffraction peaks were assigned in Ni(OH)<sub>2</sub> (JPCDS 00-002-1112), and were observed in Ni/Mo<sub>x</sub>C/rGOCS. Additional diffraction peaks in the composite with melamine were assigned to Mo<sub>16</sub>N<sub>7</sub> (JPCDS 00-023-1256). The XRD patterns also gave a broadened peak near 25°, corresponding to the (002) Bragg reflection of graphite [26]. These results indicate that the carbon composites are amorphous and consist of graphite crystallites and disordered areas.

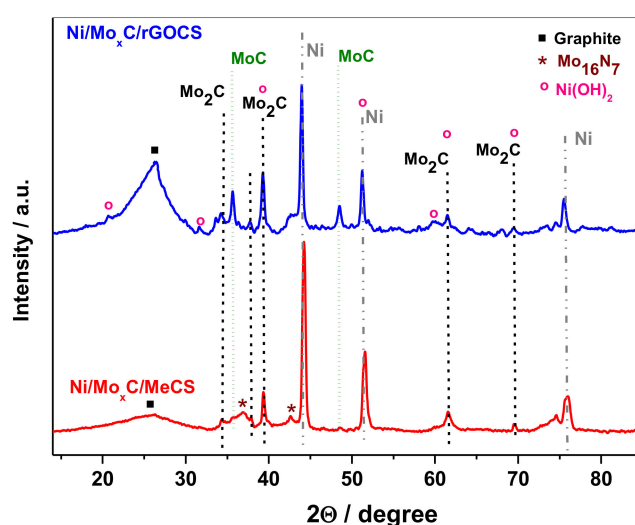


**Figure 1.** X-ray diffraction (XRD) patterns of composites.

Table 1 shows the elemental analysis and inductively coupled plasma optical emission spectrometry ICP-OES of the composites after the acid washing. The chemical analyses show similar nitrogen

content in both of the composites, hence, no additional incorporation of nitrogen was attained with melamine. Higher P loading was obtained using graphene oxide GO as carbon matrix, while the amount of Ni and Mo increased in the composite with melamine. The most significant difference between both composites is the BET specific surface area (Table 1). The carbonization of chitosan with graphene oxide leads that of the composite with a higher surface area than chitosan-melamine composite, resulting in more exposed sites for the Ni/Mo<sub>x</sub>C/rGOCS electrocatalyst.

**Table 1.** Chemical composition of the catalysts (wt%), BET surface area and Raman I<sub>D</sub>/I<sub>G</sub>.

Catalysts	C	N	P	Ni	Mo	BET (m <sup>2</sup> /g)	I <sub>D</sub> /I <sub>G</sub>
Ni/Mo <sub>x</sub> C/rGOCS	45	1.4	2.1	6.3	17	132	1.09
Ni/Mo <sub>x</sub> C/MeCS	40	1.3	0.7	8.0	22	17	0.94

The Raman spectra further confirms the graphitization degree of the catalysts (Figure 2) with the D-band (about 1340 cm<sup>-1</sup>), which is related to the presence of defects, and the G-band (about 1590 cm<sup>-1</sup>) which is associated with the vibration of sp<sup>2</sup>-bonded carbon atoms. As given in Table 1, the ratio of I<sub>D</sub>/I<sub>G</sub> of Ni/Mo<sub>x</sub>C/rGOCS shows the high value of 1.09, indicating that the internal degree of defects and disorder is larger in the chitosan-graphene composite, which is positive to the transfer of electrons [31].

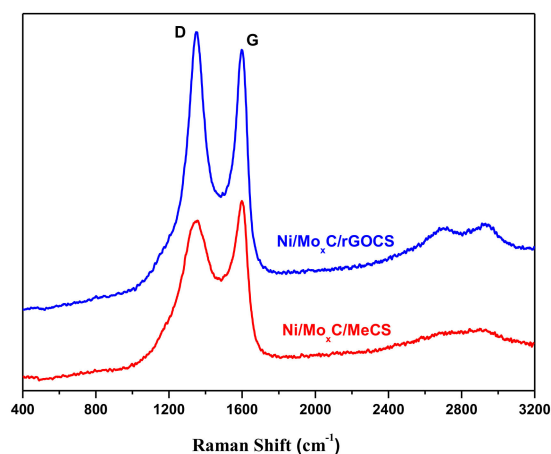


**Figure 2.** Raman spectra of Ni/Mo<sub>x</sub>C/rGOCS and Ni/Mo<sub>x</sub>C/MeCS.

Figure 3 shows the high-resolution N1s (a) and P2p (b) XPS spectra of the composites. In Figure 3a, the peak at a lower binding energy (~397 eV) is assigned to Mo3p. The peak deconvolution of Ni/Mo<sub>x</sub>C/rGOCS suggests three nitrogen components with the binding energies centered at about 398.2, 400.1, and 401.7 eV corresponding to pyridinic N, pyrrolic N, and quaternary N, respectively. The surface of the Ni/Mo<sub>x</sub>C/MeCS composite only shows the presence of two pyridinic N and pyrrolic N species. However, the peak at 397 eV could also be assigned to nitride species, indicating that the presence of Mo<sub>16</sub>N<sub>7</sub> should not be discarded. The P 2p spectra measured by XPS show a broad and low intensity peak centred at 132.5 eV in both samples, assigned to P-C (Figure 3b) [32,33]. These results imply that N and P are incorporated into the carbon matrix in both composites.

The morphology and structure of the composites were studied using a transmission electronic microscope (TEM) (Figure 4). The TEM images in Figure 4a,c show the uniform distribution of nanoparticles in the Ni/Mo<sub>x</sub>C/rGOCS and Ni/Mo<sub>x</sub>C/MeCS composites, respectively. The average particle size is estimated to be 3.5 nm for Ni/Mo<sub>x</sub>C/rGOCS and 10.6 nm for Ni/Mo<sub>x</sub>C/MeCS. The high-resolution TEM image for the Ni/Mo<sub>x</sub>C/rGOCS composite (Figure 4b) shows the presence of MoC phases (spacing of 2.47 Å corresponds to the (101) plane) and Ni(OH)<sub>2</sub> phases (spacing of 2.33 Å corresponds to the (002) plane). In the Ni/Mo<sub>x</sub>C/MeCS composite (Figure 4d), the MoC phases can

also be seen but not the  $\text{Ni}(\text{OH})_2$  phases, showing, in addition, phases of  $\text{Mo}_{16}\text{N}_7$  (spacing of 2.396 Å corresponds to the (222) plane). These results are consistent with the crystal phases shown in the XRD patterns.

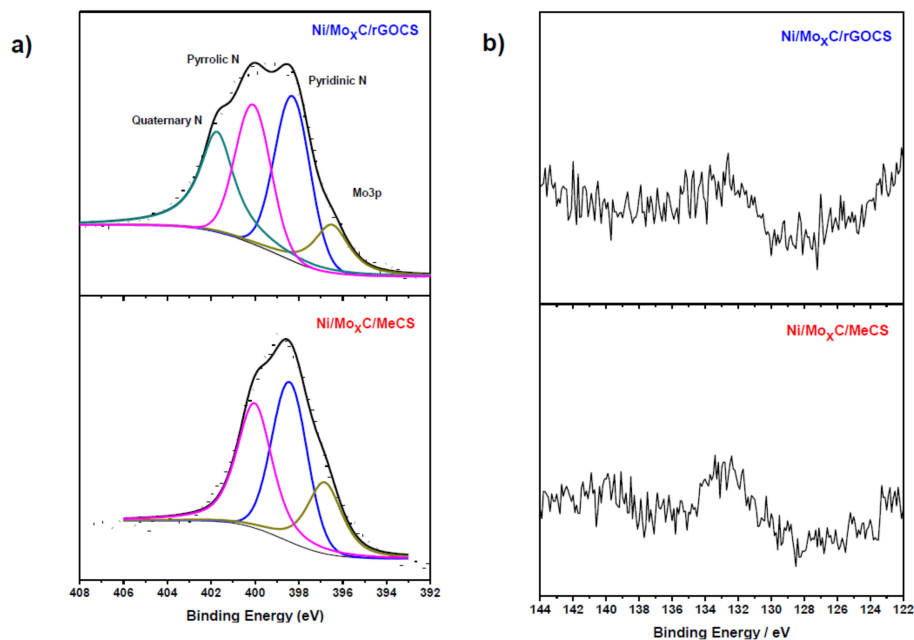


**Figure 3.** High-resolution N1s XPS spectra (a) and P2p (b) of composites.

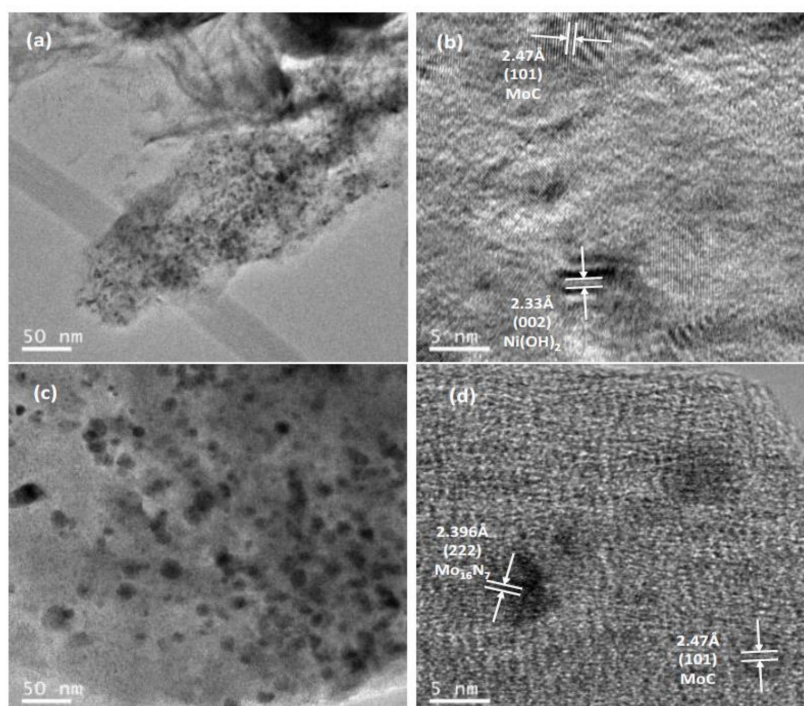


**Figure 4.** TEM and HRTEM images of the  $\text{Ni}/\text{Mo}_x\text{C}/\text{rGOCS}$  (a,b) and  $\text{Ni}/\text{Mo}_x\text{C}/\text{MeCS}$  (c,d) composites.

The OER performances of  $\text{Ni}/\text{Mo}_x\text{C}/\text{rGOCS}$ ,  $\text{Ni}/\text{Mo}_x\text{C}/\text{MeCS}$ , and  $\text{IrO}_2$  are displayed in Figure 5a. First, the catalysts were cycled 100 times at the scanning rate of  $0.10 \text{ V s}^{-1}$  between 0.05 and 1.0 V versus RHE in an Ar-saturated 0.1 M NaOH. The OER polarization curves of the catalysts were obtained by using a rotating ring-disk electrode (RRDE) at 1600 rpm. All linear sweep voltammetry (LSV)

curves were performed between 1.2 and 1.8 V with  $0.01 \text{ V s}^{-1}$  as the scan rate, and they were corrected with 48% iR-compensation. It was observed that the OER performance of the Ni/Mo<sub>x</sub>C/rGOCS and Ni/Mo<sub>x</sub>C/MeCS composites required an overpotential of 401 mV and 409 mV, respectively, to achieve a current density of  $10 \text{ mA cm}^{-2}$ . Noticeably, these overpotentials are similar to the commercial catalyst IrO<sub>2</sub> (410 mV).

Finally, a degradation test was performing by cycling 100 times in the same potential window, using  $0.1 \text{ V s}^{-1}$  as the scan rate (Figure 5b). The bottom panel of Figure 5b displays the LSV curves by the disk electrode during the anodic sweep potential, whereas, the upper panel shows the current provided by the ring electrode that is fixed at 0.4 V. This last measurement was conducted to confirm which anodic contribution is associated with the reliable oxygen evolution reaction. Therefore, the OER can be discerned with the ring signal, where other reactions such as metal oxidation are eluded. An increment of the catalytic activity towards the OER is observed in both figures (bottom and upper panels of Figure 5b) and follows the subsequent order, Ni/Mo<sub>x</sub>C/MeCS > Ni/Mo<sub>x</sub>C/rGOCS. As shown in the upper panel of Figure 5b, there is no current at the ring electrode until 1.5 V potential, which indicates that the anodic current delivered by the disk is related to other species than molecular oxygen [34]. According to this, Ni/Mo<sub>x</sub>C/rGOCS develops an anodic peak at 1.41 V, which is attributed to the oxidation of Ni(II) to Ni(III) [13]. Ni/Mo<sub>x</sub>C/MeCS also displays a broad oxidation peak of approximately 1.44 V, which overlaps with further oxidation of the metal, and with the beginning of the oxygen evolution process. Furthermore, the ring signal before and after the degradation test does not show any displacement of OER performance in Ni/Mo<sub>x</sub>C/rGOCS, however, the upper panel clearly shows a shift of the onset potential at high potential values in Ni/Mo<sub>x</sub>C/MeCS.

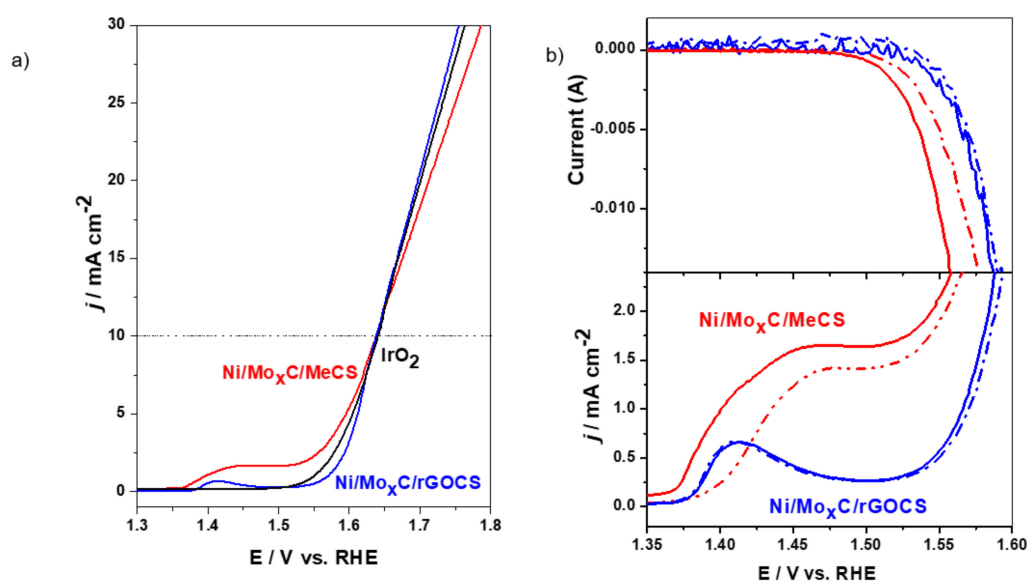
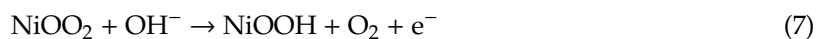
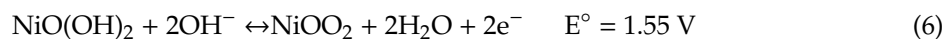


**Figure 5.** OER activities in 0.1 M NaOH at 1600 rpm (a) composites and IrO<sub>2</sub> and (b) before (—) and after degradation test (···) of composites. Low panel: disk signal recorded at  $10 \text{ mV} \cdot \text{s}^{-1}$ , top panel: the current of the ring recorded at 0.4 V.

It is known that at potentials above 0.1 V there is Ni(II) formation on the Ni electrode surface in an alkaline solution in Ni-based electrocatalysts, which causes the partial passivation of the electrode surface to form Ni/Ni(OH)<sub>2</sub> [35]. The anodic potential sweep results in the formation of two characteristic peaks in the voltammogram close to 1.35 V and 1.5 V, which correspond to the oxidation of ordered Ni(OH)<sub>2</sub> phase to hydrous Ni(III) oxide (NiOOH phase), and to further oxidation of surface

Ni(III) to Ni(IV) state along with the OER, respectively [35–37]. The OER mechanism of the Ni-based electrocatalysts in alkaline solution typically consists of three elementary steps [35].



Therefore, hydrous NiOOH is the main phase that takes part in the overall process, which should be recuperated on the electrocatalyst surface after the sequence of reaction. In Ni/Mo<sub>x</sub>C/rGOCS the conversion of Ni(OH)<sub>2</sub> to NiOOH at 1.41 V indicates that Ni(III) is the actual catalytic center to the OER, which also remains stable after the stability test. However, it seems that Ni(OH)<sub>2</sub> is less stabilized in Ni/Mo<sub>x</sub>C/MeCS and is not completely recovered after the degradation test (Figure 5b), which appears to be related to a shift of the onset potential in the ring signal. Additionally, the direct role of Mo<sub>x</sub>C should be considered. The synergistic effect between molybdenum carbide and Ni has also been observed before [13,19]. The Mo<sub>x</sub>C/Ni heterostructures contributes to the formation of in situ NiOOH/NiO(OH)<sub>2</sub> and molybdenum species during the anodic process, increasing the active sites exposed on the composites and promoting the OER performance. The N- and P-dual doped carbon matrices also modify the composites electronic properties improving the charge transfer, facilitating chemisorption of the OH<sup>-</sup> species, and stabilizing the Mo<sub>x</sub>C structures [22]. The mechanism of stabilization of Mo<sub>x</sub>C/Ni(OH)<sub>2</sub> nanoparticles in the Ni/Mo<sub>x</sub>C/rGOCS composite may be due to the higher surface area of the graphene carbon matrix, which allows a better introduction of N and P centers in the graphene structure and increases the internal degree of defects and disorder of the composite.

### 3. Materials and Methods

Ultrapure water (18.2 MΩ cm) was used in all the experiments (Milli-Q®, Millipore). In typical experiments, chitosan (low molecular weight, Sigma Aldrich) was dissolved in 2 wt.% acetic acid solution (Glacial, Sigma Aldrich) under stirring at 25 °C. An appropriate amount of NiCl<sub>2</sub> (Merck) in water solution was added drop-by-drop to the solution of chitosan in acetic acid (solution A). The GO was dispersed into water with an ultrasonic treatment, where the pH was adjusted with concentrated acetic acid (solution B1). The melamine solution was prepared in a similar way (solution B2). Then, solution A was slowly added to solution B1 or B2 and was stirred vigorously for 2 h at room temperature. Afterwards, molybdophosphoric acid solution, H<sub>3</sub>PMo<sub>12</sub>O<sub>40</sub> (ACS reagent, Sigma Aldrich), was added to the mixture. After two hours of stirring, the mixture was dried at 70 °C in a vacuum oven. The samples were pyrolyzed in a quartz tubular at 800 °C for 3 h under N<sub>2</sub> atmosphere with a heating ramp of 4 C min<sup>-1</sup>. The composites were washed in an HCl solution (10 wt%) for 3 h. The final samples were filtered and washed with H<sub>2</sub>O until free of chlorine ions. Finally, the catalysts were dried at 70 °C in a vacuum oven. The two catalysts were labelled Ni/Mo<sub>x</sub>C/rGOCS and Ni/Mo<sub>x</sub>C/MeCS. For comparison, IrO<sub>2</sub> (Sigma Aldrich) was used as reference.

Metal loadings of the composites were determined using inductively coupled plasma optical emission spectrometry (ICP-OES) with a Perkin-Elmer Optima 3300 DV spectrometer. Elemental analysis was tested in a LECO CHNS-932. A PANalytical X'Pert Pro X-ray diffractometer with a Cu Kα source was used to obtain the X-ray diffraction profiles of the powder composites. The X-ray photoelectron spectroscopy (XPS) spectra of the catalysts were acquired using an OMICRON ESCA+ spectrometer with dual x-ray source (MgKα = 1253.6 eV, AlKα = 1486.6 eV).

Raman spectroscopy were obtained with a Renishaw in Via Raman microscope spectrometer equipped with a laser beam emitting at 532 nm and 5 mW output power. Transmission electronic microscope (TEM) images were performed using a HRTEM JEOL 2100F operating at an accelerating voltage of 200 kV.

Electrochemical procedures were performed at room temperature using a three-electrode system managed by a potentiostat/galvanostat AUTOLAB PGSTAT302N. For all electrochemical measurements the three-electrode system was composed of a glassy carbon rod as the counter electrode and a reversible hydrogen electrode (RHE) as the reference electrode. For the working electrode a rotating ring-disk electrode (RRDE) was employed which was composed of a glassy carbon disk with 0.196 cm<sup>2</sup> of area and a Pt ring. The working electrode was prepared by adding 30 µL of catalytic ink, prepared by dispersing 4 mg of catalyst in 385 µL of IPA:H<sub>2</sub>O (1:1) solution and 15 µL of Nafion<sup>®</sup> (5 wt.%, Sigma-Aldrich) as binder. The supporting electrolyte was 0.1M NaOH aqueous solution. For all measurements, N<sub>2</sub> (99.99%, Air Liquid) was employed to make an inert environment.

#### 4. Conclusions

In summary, we developed a new one-step synthesis strategy of multi-active site composites based on Ni and molybdenum carbide embedded in N- and P-dual doped carbon matrices. Chitosan biopolymer was used as the carbon and nitrogen source, and molybdophosphoric acid as the P and Mo precursor. Two composites were obtained through annealing at 800 °C in a mixture of chitosan with two unlike carbon matrices, melamine or graphene oxide. Both composites showed good OER activity similar to IrO<sub>2</sub> in an alkaline medium, attributed to the synergic effect of Mo<sub>x</sub>C/Ni(OH)<sub>2</sub> structures, which are stabilized by N- and P-dual doped carbon matrices. The enhanced durability of Ni/Mo<sub>x</sub>C/rGOCS was due to the higher surface area and internal degree of defects and the disorder of the graphene composite. N- and P-dual doped carbon matrices modified the composite electronic properties improving the charge transfer, facilitating chemisorption of the OH<sup>-</sup> species, and stabilizing the Mo<sub>x</sub>C structures. This finding offers electrocatalysts of low cost and suitable activity from chitosan renewable material. It could also provide a general approach to design the electrochemical features of other transition-metal carbides-based carbon composites for various electrochemical applications.

**Author Contributions:** B.A. conceptualization, methodology, investigation, materials; J.M.L.-C. experimentation, data interpretation; M.C.-S. analysis, interpretation; M.J.L.E. review, funding acquisition, suggestions; M.V.M.-H. supervision, logical interpretation, writing—review and editing.

**Funding:** By the Spanish Ministry of Science, Innovation and Universities, through project ENE2017-83976-C2-1-R (co-funded by FEDER), the Spanish National Research Council (CSIC) through project iCOOP20202 and MERC grant project 99392002.

**Acknowledgments:** J.M. Luque also thanks the Spanish Ministry of Science, Innovation and Universities for his Ph.D. grant.

**Conflicts of Interest:** The authors declare no conflict of interest.

#### References

1. Barbir, F. PEM electrolysis for production of hydrogen from renewable energy sources. *Sol. Energy* **2005**, *78*, 661–669. [[CrossRef](#)]
2. Wurster, R.; Schindler, J. Solar and wind energy coupled with electrolysis and fuel cells. *Handb. Fuel Cells* **2003**, *3*, 62–77.
3. Yang, Y.; Zhou, K.; Ma, L.; Liang, Y.; Yang, X.; Cui, Z.; Zhu, S.; Li, Z. Free-standing ternary NiWP film for efficient water oxidation reaction. *Appl. Surf. Sci.* **2018**, *434*, 871–878. [[CrossRef](#)]
4. Carmo, M.; Fritz, D.L.; Mergel, J.; Stolten, D. A comprehensive review on PEM water electrolysis. *Int. J. Hydrogen Energy* **2013**, *38*, 4901–4934. [[CrossRef](#)]
5. Fabbri, E.; Schmidt, T.J. Oxygen Evolution Reaction—The Enigma in Water Electrolysis. *ACS Catal.* **2018**, *8*, 9765–9774. [[CrossRef](#)]
6. Man, I.C.; Su, H.-Y.; Hansen, H.A.; Martinez, J.I.; Inoglu, N.G.; Kitchin, J.; Jaramillo, T.F.; Nørskov, J.K.; Rossmeisl, J.; Calle-Vallejo, F.; et al. Universality in Oxygen Evolution Electrocatalysis on Oxide Surfaces. *ChemCatChem* **2011**, *3*, 1159–1165. [[CrossRef](#)]
7. Seong, K.J.; Byunghoon, K.; Hyunah, K.; Kisuk, K. Recent Progress on Multimetal Oxide Catalysts for the Oxygen Evolution Reaction. *Adv. Energy Mater.* **2018**, *8*, 1702774. [[CrossRef](#)]

8. Suen, N.-T.; Hung, S.-F.; Quan, Q.; Zhang, N.; Xu, Y.-J.; Chen, H.M. Electrocatalysis for the oxygen evolution reaction: Recent development and future perspectives. *Chem. Soc. Rev.* **2017**, *46*, 337–365.
9. Slavcheva, E.; Radev, I.; Bliznakov, S.; Topalov, G.; Andreev, P.; Budevski, E. Sputtered iridium oxide films as electrocatalysts for water splitting via PEM electrolysis. *Electrochim. Acta* **2007**, *52*, 3889–3894. [[CrossRef](#)]
10. Zhang, Y.; Shao, Q.; Long, S.; Huang, X. Cobalt-molybdenum nanosheet arrays as highly efficient and stable earth-abundant electrocatalysts for overall water splitting. *Nano Energy* **2018**, *45*, 448–455. [[CrossRef](#)]
11. Yu, Y.; Hu, Q.; Xiao, W.; Wang, J.; Wang, L. Design of highly efficient Ni-based water-electrolysis catalysts by a third transition metal addition into Ni<sub>3</sub>Mo. *Intermetallics* **2018**, *94*, 99–105. [[CrossRef](#)]
12. Kim, B.; Oh, A.; Kabiraz, M.K.; Hong, Y.; Joo, J.; Baik, H.; Choi, S.-I.; Lee, K. NiOOH Exfoliation-Free Nickel Octahedra as Highly Active and Durable Electrocatalysts Toward the Oxygen Evolution Reaction in an Alkaline Electrolyte. *ACS Appl. Mater. Interfaces* **2018**, *10*, 10115–10122. [[CrossRef](#)] [[PubMed](#)]
13. Zhang, X.; Huang, L.; Han, Y.; Xu, M.; Dong, S. Nitrogen-doped carbon encapsulating  $\gamma$ -MoC/Ni heterostructures for efficient oxygen evolution electrocatalysts. *Nanoscale* **2017**, *9*, 5583–5588. [[CrossRef](#)]
14. Jahangir, M.; Polydoros-Chrysovalantis, I.; Nikolaos, L.; Panayotis, K.; Manashi, N. A Molecular Ni-complex Containing Tetrahedral Nickel Selenide Core as Highly Efficient Electrocatalyst for Water Oxidation. *ChemSusChem* **2016**, *9*, 3128–3132. [[CrossRef](#)]
15. Xiong, X.; You, C.; Liu, Z.; Asiri, A.M.; Sun, X. Co-Doped CuO Nanoarray: An Efficient Oxygen Evolution Reaction Electrocatalyst with Enhanced Activity. *ACS Sustain. Chem. Eng.* **2018**, *6*, 2883–2887. [[CrossRef](#)]
16. Gao, M.; Sheng, W.; Zhuang, Z.; Fang, Q.; Gu, S.; Jiang, J.; Yan, Y. Efficient Water Oxidation Using Nanostructured  $\alpha$ -Nickel-Hydroxide as an Electrocatalyst. *J. Am. Chem. Soc.* **2014**, *136*, 7077–7084. [[CrossRef](#)] [[PubMed](#)]
17. Louie, M.W.; Bell, A.T. An Investigation of Thin-Film Ni-Fe Oxide Catalysts for the Electrochemical Evolution of Oxygen. *J. Am. Chem. Soc.* **2013**, *135*, 12329–12337. [[CrossRef](#)] [[PubMed](#)]
18. Yu, Z.-Y.; Duan, Y.; Gao, M.-R.; Lang, C.-C.; Zheng, Y.-R.; Yu, S.-H. A one-dimensional porous carbon-supported Ni/Mo<sub>2</sub>C dual catalyst for efficient water splitting. *Chem. Sci.* **2017**, *8*, 968–973. [[CrossRef](#)]
19. Das, D.; Santra, S.; Nanda, K.K. In Situ Fabrication of a Nickel/Molybdenum Carbide-Anchored N-Doped Graphene/CNT Hybrid: An Efficient (Pre)catalyst for OER and HER. *ACS Appl. Mater. Interfaces* **2018**, *10*, 35025–35038. [[CrossRef](#)]
20. Jin, Y.; Wang, H.; Li, J.; Yue, X.; Han, Y.; Shen, P.K.; Cui, Y. Porous MoO<sub>2</sub> Nanosheets as Non-noble Bifunctional Electrocatalysts for Overall Water Splitting. *Adv. Mater.* **2016**, *28*, 3785–3790. [[CrossRef](#)]
21. Jiang, J.; Liu, Q.; Zeng, C.; Ai, L. Cobalt/molybdenum carbide@N-doped carbon as a bifunctional electrocatalyst for hydrogen and oxygen evolution reactions. *J. Mater. Chem. A* **2017**, *5*, 16929–16935. [[CrossRef](#)]
22. Anjum, M.A.R.; Lee, M.H.; Lee, J.S. Boron- and Nitrogen-Codoped Molybdenum Carbide Nanoparticles Imbedded in a BCN Network as a Bifunctional Electrocatalyst for Hydrogen and Oxygen Evolution Reactions. *ACS Catal.* **2018**, *8*, 8296–8305. [[CrossRef](#)]
23. Qiao, M.; Tang, C.; He, G.; Qiu, K.; Binions, R.; Parkin, I.P.; Zhang, Q.; Guo, Z.X.; Titirici, M. Graphene/nitrogen-doped porous carbon sandwiches for the metal-free oxygen reduction reaction: Conductivity versus active sites. *J. Mater. Chem. A* **2016**, *4*, 12658–12666. [[CrossRef](#)]
24. Rybarczyk, M.K.; Jablonska, M.; Lieder, M. N-doped mesoporous carbon nanosheets obtained by pyrolysis of a chitosan–melamine mixture for the oxygen reduction reaction in alkaline media. *RSC Adv.* **2015**, *5*, 44969–44977. [[CrossRef](#)]
25. Xu, Z.; Si, J. Preparation of N-doped Nanoporous Carbon from Crude Biomass and its Electrochemical Activity. *NANO* **2016**, *11*, 1650028. [[CrossRef](#)]
26. Aghabarari, B.; Nezafati, N.; Roca-Ayats, M.; Capel-Sánchez, M.C.; Lázaro, M.J.; Martínez-Huerta, M.V. Effect of molybdophosphoric acid in iron and cobalt graphene/chitosan composites for oxygen reduction reaction. *Int. J. Hydrogen Energy* **2017**, *42*, 28093–28101. [[CrossRef](#)]
27. Aghabarari, B.; Martínez-Huerta, M.V.; Ghiaci, M.; Fierro, J.L.G.; Peña, M.A. Hybrid chitosan derivative-carbon support for oxygen reduction reactions. *RSC Adv.* **2013**, *3*, 5378–5381. [[CrossRef](#)]
28. Selvam, S.; Balamuralitharan, B.; Jegatheeswaran, S.; Kim, M.-Y.; Karthick, S.N.; Raj, J.A.; Boomi, P.; Sundrarajan, M.; Prabakar, K.; Kim, H.-J. Electrolyte-imprinted graphene oxide–chitosan chelate with copper crosslinked composite electrodes for intense cyclic-stable, flexible supercapacitors. *J. Mater. Chem. A* **2017**, *5*, 1380–1386. [[CrossRef](#)]

29. Li, R.; Cao, A.; Zhang, Y.; Li, G.; Jiang, F.; Li, S.; Chen, D.; Wang, C.; Ge, J.; Shu, C. Formation of Nitrogen-Doped Mesoporous Graphitic Carbon with the Help of Melamine. *ACS Appl. Mater. Interfaces* **2014**, *6*, 20574–20578. [[CrossRef](#)]
30. Ma, Z.; Zhang, H.; Yang, Z.; Ji, G.; Yu, B.; Liu, X.; Liu, Z. Mesoporous nitrogen-doped carbons with high nitrogen contents and ultrahigh surface areas: Synthesis and applications in catalysis. *Green Chem.* **2016**, *18*, 1976–1982. [[CrossRef](#)]
31. Wang, M.; Dipazir, S.; Lu, P.; Wang, Y.; Yuan, M.; Li, S.; Zhang, G. Synthesis of polyoxometalates derived bifunctional catalyst towards efficient overall water splitting in neutral and alkaline medium. *J. Colloid Interface Sci.* **2018**, *532*, 774–781. [[CrossRef](#)] [[PubMed](#)]
32. Razmjooei, F.; Singh, K.P.; Bae, E.J.; Yu, J.-S. A new class of electroactive Fe- and P-functionalized graphene for oxygen reduction. *J. Mater. Chem. A* **2015**, *3*, 11031–11039. [[CrossRef](#)]
33. Razmjooei, F.; Singh, K.P.; Song, M.Y.; Yu, J.-S. Enhanced electrocatalytic activity due to additional phosphorous doping in nitrogen and sulfur-doped graphene: A comprehensive study. *Carbon* **2014**, *78*, 257–267. [[CrossRef](#)]
34. Roca-Ayats, M.; Roca-Moreno, M.; Martínez-Huerta, M. Optimization of alkaline catalytic inks for three-electrode electrochemical half-cell measurements. *Int. J. Hydrogen Energy* **2016**, *41*, 19656–19663. [[CrossRef](#)]
35. Juodkazis, K.; Juodkazytė, J.; Vilkauskaitė, R.; Jasulaitienė, V.; Juodkazis, S. Nickel surface anodic oxidation and electrocatalysis of oxygen evolution. *J. Solid State Electrochem.* **2008**, *12*, 1469–1479. [[CrossRef](#)]
36. Trotochaud, L.; Ranney, J.K.; Williams, K.N.; Boettcher, S.W. Solution-Cast Metal Oxide Thin Film Electrocatalysts for Oxygen Evolution. *J. Am. Chem. Soc.* **2012**, *134*, 17253–17261. [[CrossRef](#)] [[PubMed](#)]
37. Smith, R.D.L.; Prévot, M.S.; Fagan, R.D.; Trudel, S.; Berlinguette, C.P. Water Oxidation Catalysis: Electrocatalytic Response to Metal Stoichiometry in Amorphous Metal Oxide Films Containing Iron, Cobalt, and Nickel. *J. Am. Chem. Soc.* **2013**, *135*, 11580–11586. [[CrossRef](#)] [[PubMed](#)]



© 2019 by the authors. Licensee MDPI, Basel, Switzerland. This article is an open access article distributed under the terms and conditions of the Creative Commons Attribution (CC BY) license (<http://creativecommons.org/licenses/by/4.0/>).